JTTEE5 15:765-772
DOI: 10.1361/105996306X147045
1059-9630/$19.00 © ASM International

Exploring Thermal Spray Gray Alumina Coating Pore Network Architecture by Combining Stereological Protocols and Impedance Electrochemical Spectroscopy

G. Antou, G. Montavon, F. Hlawka, A. Cornet, and C. Coddet

(Submitted February 27, 2006; in revised form July 29, 2006)

Complex multiscale pore network architecture characterized by multimodal pore size distribution and connectivity develops during the manufacture of ceramic thermal spray coatings from intra- and interlamellar cracks generated when each lamella spreads and solidifies to globular pores resulting from lamella stacking defects. This network significantly affects the coating properties and their in-service behaviors. De Hoff stereological analysis permits quantification of the three-dimensional (3D) distribution of spheroids (i.e., pores) from the determination of their two-dimensional (2D) distribution estimated by image analysis when analyzing the coating structure from a polished plane. Electrochemical impedance spectroscopy electrochemically examines a material surface by frequency variable current and potential and analyzes the complex impedance. When a coating covers the material surface, the electrolyte percolates through the more or less connected pore network to locally passivate the substrate. The resistive and capacitive characteristics of the equivalent electrical circuit will depend upon the connected pore network architecture. Both protocols were implemented to quantify thermal spray coating structures. Al_2O_3-13TiO_2 coatings were atmospherically plasma sprayed using several sets of power parameters, arc current intensity, plasma gas total flow rate, and plasma gas composition in order to determine their effects on pore network architecture. Particle characteristics upon impact, especially their related dimensionless numbers, such as Reynolds, Weber, and Sommerfeld criteria, were also determined. Analyses permitted identification of (a) the major effects of power parameters upon pore architecture and (b) the related formation mechanisms.

Keywords connected pore, crack, electrochemical impedance spectroscopy, globular pore, image analysis, pore network, stereology, thermal spray coating structure

1. Introduction

A thermal spray coating resulting from the stacking of microstructural units called splats exhibits a highly anisotropic lamellar structure. Moreover, stacking defects generate specific interlamellar features within the structure, mainly pores, which may be connected to the upper surface of the coating. In addition, peripheral decohesions around lamellae induce delaminations between the lamellae. Interlamellar microscopic cracks may also arise due to rapid solidification process of the particles subsequent to their spreading (Ref 1) after impact. This behavior is emphasized for ceramic materials that exhibit high shrinkage stresses. These features generate an interconnected network of pores from which result the coating permeability.

This pore network may (a) limit the coating performance in service (Ref 2) because the substrate material can react with any medium that penetrates through the structure (i.e., corrosion occurs at the substrate/coating interface and leads to coating spallation; Ref 3) or (b) enhance the coating performance in service because they provide compliance to strains and lower the thermal conductivity by generating thermal resistance within the structure (i.e., the case of thermal barriers). Nevertheless, engineers often consider the complex pore network only in terms of level and much less often in terms of architecture.

The pore network architecture of a ceramic coating, i.e., Al_2O_3-TiO_2 (13% by weight), was quantified by implementing easily available and familiar protocols, namely, image analysis (IA) coupled with stereological protocols and electrochemical impedance spectroscopy (EIS), and the effects of several major spray operating parameters upon pore network generation were identified.

This article was originally published in *Building on 100 Years of Success, Proceedings of the 2006 International Thermal Spray Conference* (Seattle, WA), May 15-18, 2006, B.R. Marple, M.M. Hyland, Y.-Ch. Lau, R.S. Lima, and J. Voyer, Ed., ASM International, Materials Park, OH, 2006.

G. Antou, SPCTS UMR, CNRS 6638, Faculty of Sciences, University of Limoges, 123 Avenue Albert Thomas, 87 060 Limoges Cedex, France and LGECO-GLISS, INSA Strasbourg, 24 Boulevard de la Victoire, 67 000 Strasbourg, France; **G. Montavon,** SPCTS UMR, CNRS 6638, Faculty of Sciences, University of Limoges, 123 Avenue Albert Thomas, 87 060 Limoges Cedex, France; **F. Hlawka** and **A. Cornet,** LGECO-GLISS, INSA Strasbourg, 24 Boulevard de la Victoire, 67 000 Strasbourg, France; and **C. Coddet,** LERMPS, UTBM, Site de Sévenans, 90 010 Belfort Cedex, France. Contact e-mail: ghislain.montavon@unilim.fr.

2. Experimental Protocols

2.1 Feed Stock Material and Substrate

Fused and crushed gray alumina (Al_2O_3-TiO_2 13% by weight, METCO 130, Sulzer-Metco, Wohlen, Switzerland) of

Table 1 Spray operating parameters for the Metco 130 system

	Variable operating spray parameters					
	I, A	H_2, SLPM	Ar, SLPM	Ar+H_2, SLPM	H_2/Ar, %	*P*, kW
Ref	530	10.8	43.2	54	25	32.5
I	350	10.8	43.2	54	25	22.5
	700	10.8	43.2	54	25	42.0
H_2/Ar	530	4.9	49.1	54	10	27.5
	530	13.4	40.6	54	33	34.0
Ar+H_2	530	8.0	32.0	40	25	30.1
	530	14.0	56.0	70	25	35.2

Constant operating spray parameters	
Injector diameter, D_{inj}, mm	1.8
Injection distance, I_D, mm	6
Carrier gas flow rate (Ar), SLPM	3.2
Relative injector position/gun motion	Parallel
Spray distance, S_D, mm	125
Spray angle, α, deg.	~90
Spray velocity, S_V, mm s^{-1}	250
Scanning step, SS, mm $pass^{-1}$	6

pseudo-Gaussian (with a pronounced tail toward high diameters) particle size distribution ranging from +25.0 to −58.4 μm (average value, 38.4 μm) was selected as feed stock.

Substrates made of low carbon steel (S145) button-type substrates, 25 mm diameter and 20 mm height, were used. Prior to spraying, they were degreased by immersion in ethanol vapors and manually grit-blasted using α-alumina white corundum of 500 μm average particle size. After grit-blasting, they exhibited ~5 μm average roughness (Ra) and 37 μm maximum peak-to-valley height (R_{ymax}).

2.2 Spray Processing Parameters

The power parameters, namely the arc current intensity (*I*), the plasma gas total flow rate (Ar + H_2), and the hydrogen ratio (H_2/Ar), were varied to study their respective influence on the coating structural attributes; other operating spray parameters were kept at reference values (Table 1).

During coating manufacturing, substrates were cooled down at their front and back sides by dry compressed air. This permitted their average temperature to remain almost constant, in the range of 90-110 °C [measured using infrared (IR) pyrometry on the front side of the samples], in whatever other operating parameter were used.

2.3 In-Flight Particle Characteristics Upon Impact

The temperature, velocity, and diameter particle characteristics at the spray distance were measured implementing a DPV2000 analyzer (Ref 4, 5) from Tecnar (St-Bruno, QC, Canada).

The particle trajectories depend upon the operating parameters, especially the power and injection parameters. The in-flight particle average characteristics were diagnosed at the spray distance in the center of the flow pattern; i.e., at the location where the highest intensity is detected by the sensor, at a powder feed rate of 22 g min^{-1}. The average volume for data collection is several tens of cubic micrometers. The measurements are, moreover, based on the assumption that the particles behave as gray bodies, and only molten (i.e., warm) particles are detected.

Each measurement was repeated twice at 15 min intervals. In between, the plasma gun was operated with other process parameters. In effect, previously published studies emphasized an effect concerning the temporal fluctuations of processing spray parameters, especially those of arc current, plasma gun electrode wear state, etc. (Ref 6, 7). In these experiments, no significant differences were detected between the first and the second measurements. Thus the first measurement data was considered for analysis in this study.

2.4 Spreading Particle Characteristics

The literature indicates that splat formation depends upon the particle impact temperature and velocity. Particle viscosity can be related to impact temperature and particle momentum to impact velocity (Ref 8).

Several analytical models (Ref 9, 10), among other models (Ref 11), describe the flattening stage of a particle impinging normally to a smooth substrate. In this case, lamella solidification is assumed to be independent from flattening. Moreover, high pressures occur during the initial microseconds of the flattening process (Ref 12), and these models consider incompressible liquids.

Under these assumptions, the impacting particle may (a) rebound, (b) spread, (c) spread and partially splash, or (d) completely splash. These phenomena are related to critical values of the dimensionless Sommerfeld criterion, *K*, defined as:

$$K = \sqrt{\mathrm{We}\sqrt{\mathrm{Re}}} \quad \text{(Eq 1)}$$

where We and Re represent the dimensionless Weber and Reynolds numbers of the impinging particle, respectively. The Reynolds number compares inertia to viscous forces, and the Weber number is an index of the inertial force to the surface tension.

These numbers are defined as follows:

$$\mathrm{We} = \frac{\rho_p d_p V_p^2}{\sigma_p} \text{ and } \mathrm{Re} = \frac{\rho_p d_p V_p}{\mu_p} \quad \text{(Eq 2)}$$

where ρ_d refers to the particle density (kg m^{-3}), d_p to the particle diameter at the impact (m), V_p to the particle velocity at the impact (m s^{-1}), σ_d to the molten particle surface tension (N m^{-1}), and μ_p to the molten particle viscosity (Pa s).

For liquid droplets, the critical values for the Sommerfeld criteria are defined as follows (Ref 8): (a) $K < 3$, rebound from the surface; (b) $3 < K < 58$, deposition on the surface; and (c) $K > 58$, deposition and splashing.

The values of ρ_d, μ_d, and σ_d used for the calculations correspond to experimentally determined values for pure alumina (Eq 3-5) (Ref 13). Of course, 13% by weight of titania should modify these values. The results that follow, therefore, are considered as approximate values:

for $2300 < T < 3200$ K

$$\rho_d = (3.15 - 1.12 \times 10^{-4}\ T)\ 10^{-3}\ (\mathrm{kg\ m^{-3}}) \quad \text{(Eq 3)}$$

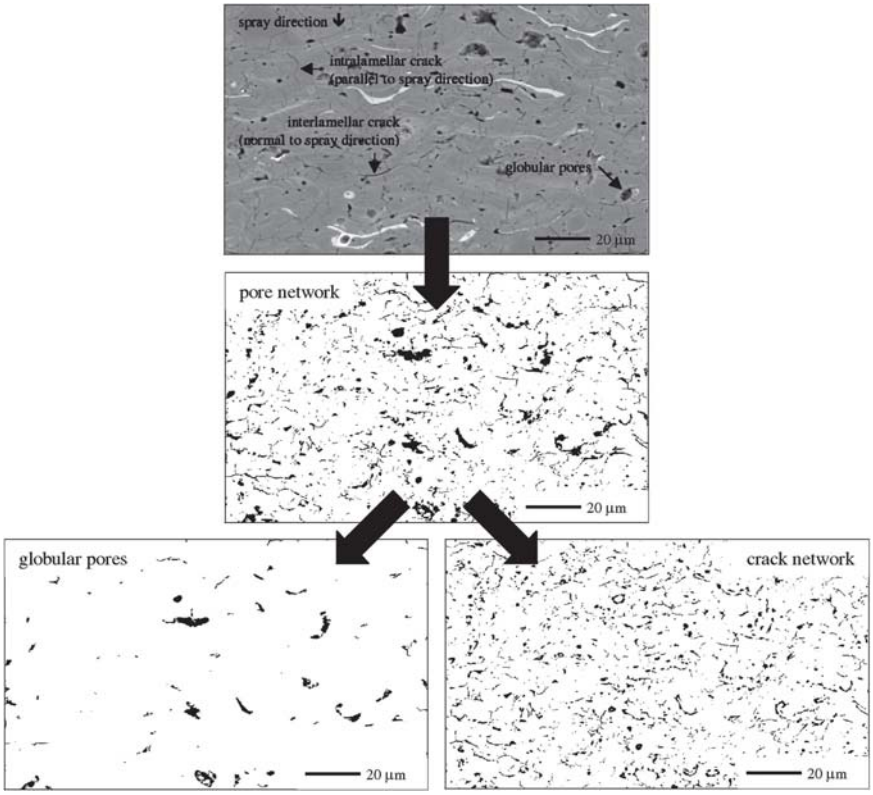

Fig. 1 IA to discriminate globular pores from the crack network

for $2300 < T < 2550$ K

$$\mu_d = 6.83 \times 10^{-8}\ \mathrm{T} \exp\left(\frac{110{,}000}{8.32T}\right)\ (\mathrm{Pa\ s}) \qquad \text{(Eq 4)}$$

for $2300 < T < 3000$ K

$$\sigma_d = (1563 - 0.5T + 43.2 \times 10^{-6}\ \mathrm{T}^2)\ 10^{-3} \times (\mathrm{N\ m^{-1}}) \qquad \text{(Eq 5)}$$

2.5 Coating Structural Observation

The samples were cut parallel to the spray direction using a diamond saw in an oil medium, mounted in rings, and infiltrated with epoxy (i.e., impregnation technique). They were then polished following standard metallographic techniques (i.e., prepolishing and diamond slurry polishing) on an automatic polishing system. Prior to scanning electron microscopy (SEM) observation (Philips XL 30 SEM, Eindhoven, The Netherlands), a carbon layer was deposited by sputtering onto the polished samples. The image resolution was 0.14 µm per pixel.

Image Analysis (IA) and Stereological Protocols. SEM images were discretized and analyzed using Image 1.62 software from NIMH (Research Services Branch of the National Institute of Mental Health, Bethesda, MD).

First, IA permitted the quantification of the overall porosity level and the crack network orientation (i.e., the Delesse protocol; Ref 14). Pores and cracks were isolated implementing several filtering and morphological protocols (Fig. 1). Pores were then analyzed in terms of numbers and relative surfaces and cracks in terms of cumulated lengths and orientations. Interlamellar (perpendicular to spray direction) and intralamellar (parallel to spray direction) cracks were discriminated and analyzed separately. The cumulated length of cracks per unit surface, L_A (m^{-1}), was calculated to deduce the cumulated surface of cracks per unit volume, A_V (m^{-1}), according to the following stereological relationship (Ref 15):

$$A_V = \frac{4}{\pi} L_A \qquad \text{(Eq 6)}$$

In addition, the De Hoff protocol for ellipsoidal particles (Ref 16, 17), derived from Schwartz-Saltykov analysis (Ref 18) for spherical particles, permitted analysis of the porosity size distribution (i.e., repartition of the porosity relative volume in each size class). Each pore two-dimensional (2D) in the plane of observation is assimilated to an ellipse of major axis (M), minor axis (m), and axial ratio ($q = m/M$). Pores in volume three-dimensional (3D) are then modeled as ellipsoids of revolution by rotation of the ellipses around their minor axis (i.e., oblate ellipsoids). Pores and cracks were then divided into 15 size classes. The increment of size class, Δ, was equal to $M_{max}/15$, where M_{max} is the highest ellipse major axis in the largest size class.

For each size class (Δ_i), the equivalent ellipsoidal volume (V_i) and the number of ellipsoidal particles per volume unit (N_{Vi}) were determined as follows:

$$V_i = \frac{\pi}{6} \cdot (M_{\max \cdot i})^3 \cdot \overline{q_i} \qquad \text{(Eq 7)}$$

$$N_{V_i} = \frac{(N_A)_i}{M_i \cdot k_i} \qquad \text{(Eq 8)}$$

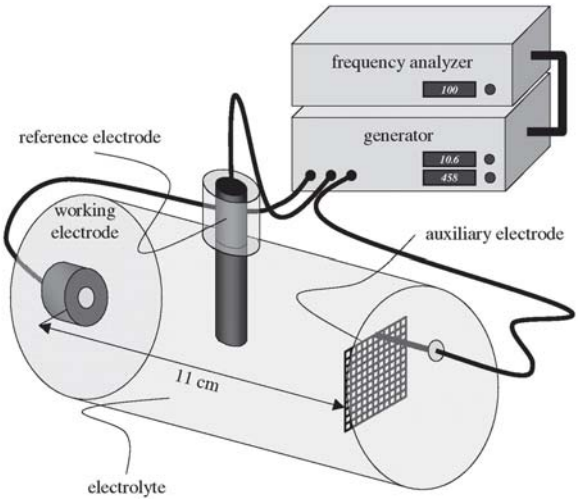

Fig. 2 EIS cell configuration

where $M_{\max\ i}$ is the maximum major axis for the considered size class, $\overline{q_i}$ the average axial ratio, $(N_A)_i$ the number of pores per image area, $\overline{M_i}$ the average major axis, and $\overline{k_i}$ the average De Hoff shape factor. The De Hoff shape factor (k) for oblate ellipsoids was defined by:

$$k(q) \int_0^{\frac{\pi}{2}} \int_0^{\frac{\pi}{2}} \frac{\sqrt{1 + (q^2 - 1) \cdot \cos^2 \phi}}{\frac{\pi}{2}} \cdot \sin \phi \cdot d\phi \cdot d\theta \qquad \text{(Eq 9)}$$

where q represents the average ellipse elongation ratio.

Thus it is possible to calculate the porosity relative volume (V_{Vi}) for each size class:

$$V_{V_i} = V_i \cdot N_{V_i} \qquad \text{(Eq 10)}$$

For each processing parameter set, the results were averaged from 15 fields of view randomly selected across the corresponding polished cross section.

Electrochemical Impedance Spectroscopy (EIS). In this study, EIS permits the quantification of the coating connected porosity level because the measurement of the porosity level via the cross-section observation, for example, by IA, permits only quantification of the porosity level and not the network connectivity. In this test, electrolyte passivates the substrate more or less after having impregnated the coatings through their connected pore networks.

EIS measurement was performed at room temperature in an EG&G PARC Model K0235 (AMETEK Princeton Applied Research, Oak Ridge, TN) flat cell of 300 mL volume (Fig. 2). The sample was used as the working electrode (exposed area of 1 cm^2). A platinum mesh was used as a counter electrode, and an Ag/AgCl electrode was used as a reference. A 0.01 mol L^{-1} $K_3Fe(CN)_6/K_4Fe(CN)_6$ aqueous solution was selected as electrolyte due to its highly reversible electrochemical exchange current density and its minimal interference with the system (i.e., gray alumina is inert with respect to this electrolyte; Ref 19).

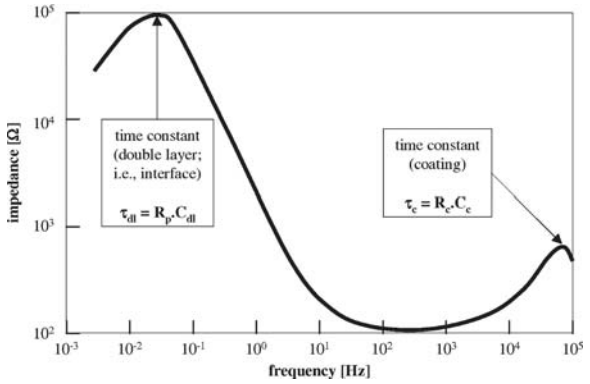

Fig. 3 Typical Bode diagram for low carbon steel coated with an Al_2O_3-13TiO_2 plasma spray coating: τ_{dl}, time constant of the double layer (i.e., electrolyte/substrate interface); R_p, polarization resistance; C_{dl}, double-layer constant phase element (CPE); τ_c, time constant of the coating; R_c, coating resistance; and C_c, coating CPE

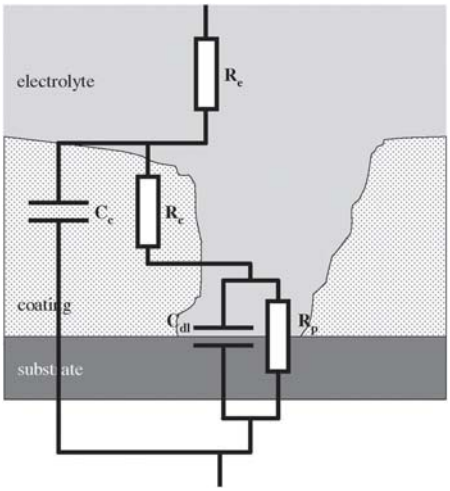

Fig. 4 Equivalent electrical circuit: R_e, electrolyte resistance; R_p, polarization resistance; C_{dl}, double layer CPE; R_c, coating resistance; and C_c, coating CPE

The three-electrode system was connected to an EG&G Model 263A EIS measurement system. A sinusoidal voltage perturbation of 10 mV amplitude and of a frequency range from 1 mHz to 100 kHz was input to the system.

Measured diagrams are associated to physical concepts that can be described by equivalent electrical circuits that take into account electrolyte resistance, pore and coating resistances, the double-layer capacitance and resistance, and the diffusive phenomena (Ref 20). In the case of an uncoated substrate, the equivalent electrical circuit generally used to depict the electrochemical reactions at the electrolyte/substrate interface is a Randles cell associated to a Warburg impedance to model the diffusion phenomenon. In the case of a coated substrate, two peaks appear on the Bode diagrams (Fig. 3) that involve the selection of a circuit including two time constants (Fig. 4). The measured diagrams did not describe a perfect capacitance for the double layer (i.e., in the Nyquist diagrams, Fig. 5, the arc of circle are not centered on the real impedance axis but present

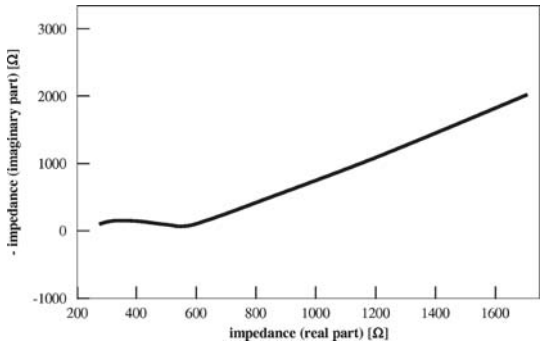

Fig. 5 Typical Nyquist diagram for low carbon steel coated with an Al_2O_3-13TiO_2 plasma spray coating

angular shifts). As a result, the capacitances were replaced by constant phase elements (CPE) (Ref 20, 21). A method to determine the open porosity level (i.e., volume ratio of connected pores, $V_{\text{connected pores}}$, over the whole coating volume, V_{total}) consists in calculating the polarization resistance ratio of uncoated (Rp_{uncoated}) and coated (Rp_{coated}) surfaces. Considering ρ_E as the electrolyte resistance (Ω m), d_{dc} as the double-layer thickness at the electrolyte/substrate interface (m), S_{total} as the uncoated surface (m^2), and S_{coated} as the substrate surface in contact with the electrolyte when the surface is coated (m^2), the open porosity level can be expressed as follows:

$$\frac{Rp_{\text{uncoated surface}}}{Rp_{\text{coated surface}}} = \frac{\rho_E \dfrac{d_{dc}}{S_{\text{total}}}}{\rho_E \dfrac{d_{dc}}{S_{\text{coated}}}} = \frac{S_{\text{coated}}}{S_{\text{total}}} \approx \frac{V_{\text{connected pores}}}{V_{\text{total}}} \qquad \text{(Eq 11)}$$

As a matter of fact, after reduction, this ratio corresponds to the coated contact surface divided by the whole contact surface (uncoated). By assuming that the S_{coat}/S_{total} ratio is equal to the volume ratio of connected pores over the whole coating volume, $V_{\text{connected pores}}/V_{\text{total}}$ (transition from a two-dimensional to a three-dimensional view implementing the Delesse stereological protocol), the open porosity level can be quantified. All the measurements were conducted on five specimens manufactured during the same run to ensure reproducibility.

One uncertainty in measurements can be induced by poor sample surface wetting by the electrolyte. In such a case, air pockets adsorb at the surface sample. Careful examinations did not reveal such a phenomenon, however. Besides, concerning the limit dimension of pores and cracks that can be characterized implementing electrochemical test, the Washburn equation permits the pore diameter (d), the pressure (p), the water surface tension ($\gamma = 72.8 \times 10^{-3}$ N m^{-1}), and the contact angle between water and pore surface ($\theta = 59°$ between water and alumina; Ref 22) to be linked as follows:

$$pd = -4\gamma \cos\theta = 1.48 \text{ nm (at atmospheric pressure)} \qquad \text{(Eq 12)}$$

So, in a first approximation, it seems that the entire pore-crack network of thermal spray coatings can be characterized by this protocol because the low water surface tension permits to impregnate a priori the thinner pores (i.e., microcracks <0.1 μm thick). The quantified interconnected pore network controls the coating impermeability and therefore the reaction of the metallic substrate to a corrosive environment.

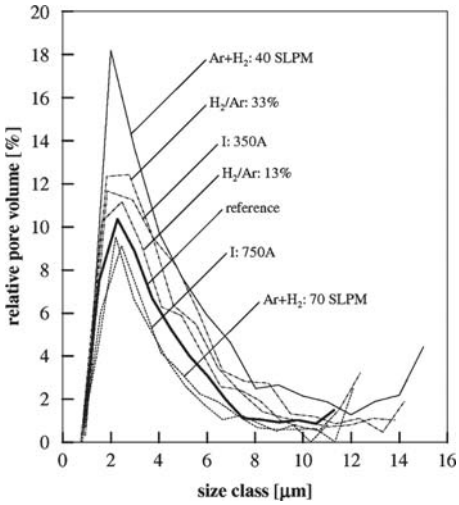

Fig. 6 Pore size distribution by De Hoff analysis

All measurements were conducted on five specimens sprayed during the same run to ensure reproducibility. Results were then averaged.

3. Results and Analyses

3.1 Pore Network Architecture

The porosity level, the repartition, and the linear density of cracks have been quantified using IA (Table 2).

Increasing the current arc intensity or the plasma gas flow rate led to an increase in the plasma average net power. Consequently, its capacity to transfer higher heat and momentum quantities to the feed stock particles is enhanced. Particle spreading is hence improved (i.e., its flattening ratio increases), which enhances the filling of gaps and anfractuosities. Finally, the porosity level decreases. Increasing the hydrogen flow rate leads to an increase of the plasma enthalpy and its thermal conductivity. Consequently, the impinging particles impact in an "over-molten" state. This induces especially a splashing of the droplets due to lower surface tension. Finally, the porosity level increases.

The De Hoff protocol permits quantification of the porosity size distributions (Fig. 6), which are bimodal in a first approximation. The first peak is centered on a pore characteristic size of 2-3 μm: it corresponds to microcracks and small globular pores. The second peak ranges from 11 to 15 μm, depending on the operating parameters, and corresponds to large globular pores.

From these distributions, it is possible to distinguish three types of porous architecture: (a) the curves under the reference operating parameters (which correspond to a reduced porosity level); (b) the curves above the reference operating parameters (which correspond to an increased porosity level); (c) the curves largely above the reference operating parameters (which correspond to a high porosity level). These pore architectures results

Table 2 Crack pore network characteristics by Delesse analysis and corresponding in-flight particle and particle spreading characteristics vs. operating parameters

Operating parameters			In-flight particle characteristics		Particle spreading characteristics						Coating pore network characteristics(a)					
I, A	Ar+H_2, SLPM	H_2/Ar, %	*V*, m s^{-1}	*T*, °C	ρ, kg m^{-3}	μ, Pa s	*ν*, N m^{-1}	Re, –	We, –	*K*, –	Total, %	SD, %	Globular, %	SD, %	Crack, %	SD, %
530	54	25	256	2324	2890	0.047	0.63	600	15377	614	6.3	0.3	1.5	0.1	4.8	0.2
350	54	25	226	2157	2908	0.068	0.69	370	8357	401	7.3	0.3	2.1	0.1	5.1	0.1
700	54	25	282	2458	2875	0.036	0.59	845	23801	832	5.8	0.2	1.2	0.1	4.5	0.1
530	54	10	216	2196	2904	0.062	0.67	385	8307	404	6.3	0.5	1.8	0.2	4.6	0.3
530	54	33	275	2384	2883	0.042	0.62	721	19824	730	7.3	0.3	1.9	0.2	5.3	0.1
530	40	25	245	2304	2892	0.049	0.64	551	13502	563	8.6	0.4	3.3	0.3	5.3	0.1
530	70	25	269	2347	2887	0.045	0.63	658	17695	674	5.3	0.3	1.1	0.1	4.2	0.1

(a) SD, standard deviation

mostly from the in-flight particle characteristics (Table 2). Increasing the plasma gas flow rate (from 54 to 70 N L min^{-1}) or the arc intensity (from 530 to 700 A) induce a lower porosity level. In turn, the Reynolds number increases by 10 and 41%, respectively. Particle spreading is hence improved, which enhances the filling of gaps and anfractuosities. Finally, the globular porosity level decreases by ~20%. The reduction of the interlamellar crack linear density is linked to higher particle flatting ratios, which favor better interlamellar contact.

For higher arc intensity, the significant increases of the Weber dimensionless number and the Sommerfeld criterion (by 55 and 36%, respectively) induce the fragmentation of the lamellae. In such a way, volume reduction consecutive to solidification of fragmented lamellae and the induced quenching stresses relaxed by vertical cracking are diminished: the resulting vertical crack linear density is reduced by ~28%.

Reducing arc current intensity (to 350 A) or increasing hydrogen ratio (from 10 to 33%) induces a higher porosity level. When the arc current intensity is decreased, the resulting higher globular porosity level of 42% can be explained by a lower Reynolds number (decrease of 38%). In this case, particles do not spread well and do not fill surface anfractuosities.

As the Reynolds number decreases, the particles spread less. This in turn creates weaker interlamellar contacts and hence increases the interlamellar crack linear density (by 37%). The higher intralamellar crack linear density seems to be due to numerous unmolten particles into the coating, which is linked to a lower particle average temperature (decrease of 7%). When the hydrogen ratio decreases, the 36% decrease in the Reynolds number may explains the higher globular porosity level (increase of 42%) and the higher horizontal crack linear density (increase of 37%), respectively linked to a lower lamella crushing and a lower interlamellar contact. As the particle temperature decreases by 6%, particles have lower quenching stresses to relax, which leads to a lower intralamellar crack linear density (decrease of 48%). On the other hand, when the hydrogen rate increases, the Weber dimensionless number and Sommerfeld criterion increase by 29 and 19%, respectively. This induces a splashing of the droplets, which increases the globular porosity level (increase of 31%), even if particles can spread better (Reynolds number increases by 20%). The higher parallel-to-interface and perpendicular-to-interface crack linear densities are associated to the lamella fragmentation, which generates lower inter- and intralamellar contacts when overlapped by other lamellae.

Decreasing the plasma gas flow rate (from 54 to 40 N L min^{-1}) generates a higher porosity level. In particular, the large increase of the globular porosity level (by 122%) is very likely related to a bad filling of anfractuosities due to a lower Reynolds number (decrease by 8%). This is very likely why the crack linear densities increase (by 33% for parallel-to-interface and by 20% for perpendicular-to-interface, respectively).

In conclusion, the coating architecture is derived significantly from the in-flight particle characteristics, and various spraying parameters can result in the same in-flight particle characteristics and hence to the same porous architecture.

3.2 Mechanisms Leading to the Pore Network Architecture

From previous analyses, Fig. 7 suggests relationships between the in-flight particle characteristics (Reynolds, Weber, and Sommerfeld numbers and particle temperature) and the resulting porous architecture.

The Reynolds number affects the particle spreading (and consequently anfractuosities filling and interlamellar contacts), which has impact on the globular porosity level and on the formation of inter- and intralamellar cracks, respectively (the higher the interlamellar contacts, the lower the interlamellar cracks and lamellar contacts).

The Weber number affects the particle fragmentation and, as a result, the globular porosity level. Moreover, the lamella center volume is modified by this characteristic, which influences the quenching stresses induced during solidification. It finally controls the formation of intralamellar cracks (an elevated Weber number induces high particle fragmentation, thus, a reduced lamella center volume and low quenching stresses in turn during solidification).

The Sommerfeld number affects the intralamellar cracks: it modifies the splashing of the droplets. Hence it alters the lamella center volume and influences the quenching stresses. Formation of intralamellar cracks is also affected by the particle temperature, which controls the ratio of unmolten particles and the quenching stresses.

3.3 Pore Network Connectivity

The open porosity level of analyzed gray alumina coatings is ranged from 2.5 to 4.8% (absolute values) representing hence 39-73% of the total porosity level (relative values). EIS mea-

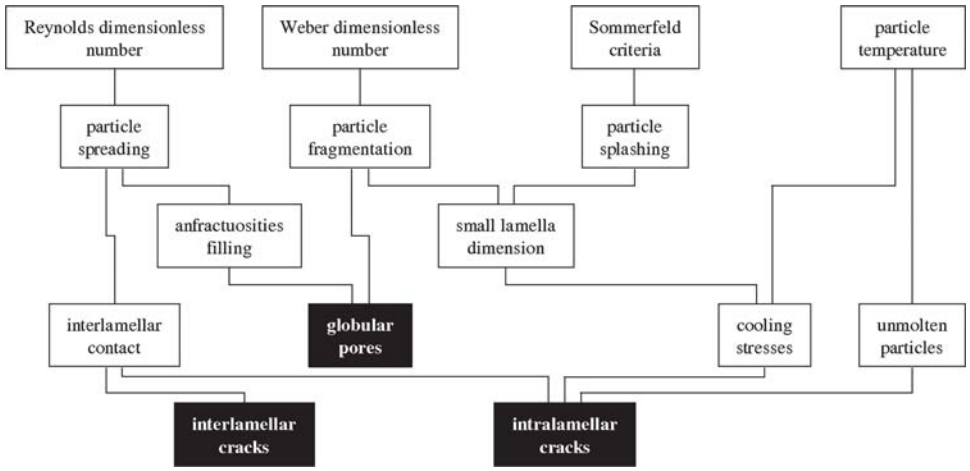

Fig. 7 Mechanisms that could lead to the formation of pore features

surements reveal that coatings containing high total porosity levels are not necessarily coatings that contain the most interconnected pores. Moreover, it seems that no correlation exists between the microcrack level and the open pore level (Fig. 8). Microcracks can be numerous without inducing a high level of connectivity. For example, for two coatings that present a "microcrack over total" porosity ratio of ~79%, the "open over total" porosity ratio varies from 47 to 64%.

Consequently, EIS permits specific quantification of the open porosity level, but no correlations have been determined between the open porosity level and the pore network characteristics measured by stereological protocols (size, shape, and orientation of the porous architecture). Nevertheless, the permeability of a coating is induced by its porous architecture. This lack of correlation can be explained by the fact that image analysis is limited by the image resolution (0.14 μm/pixel in the current study) and does not permit detection of finer microcracks, which play a relevant role in the coating pore connectivity. It can be explained also by the fact that image analysis is carried out on polished cross sections (2D view) and does not reflect the 3D character of the connected pore network. So, to study the connectivity of thermal sprayed coatings and, therefore, their eventual effects on in-service properties, EIS appears to be a well-adapted, sensitive methodology.

4. Conclusions

Thermal spray coatings derive their in-service properties from their structures. Among other structural attributes, pore network architecture plays relevant roles in the coating mechanical and chemical behaviors.

The pore network originates from the particle spreading and solidification mechanisms and from lamella stacking defects. The combination of interlamellar, intralamellar, and globular pores creates a complex pore architecture characterized by a multimodal pore size distribution and connectivity.

Al_2O_3-13TiO_2 coatings were atmospherically plasma sprayed using several sets of power parameters (arc current intensity, plasma gas total flow rate, and plasma gas composition) in order to scan their effects on the pore network architecture. In parallel, particle characteristics upon impact, especially their related dimensionless numbers such as Reynolds, Weber, and Sommerfeld criteria, were determined.

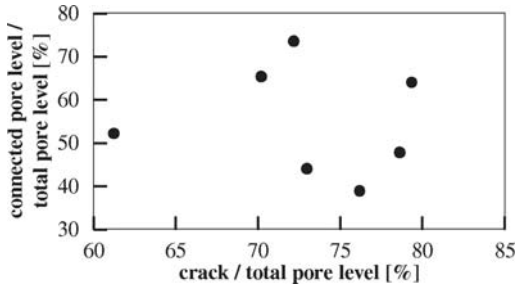

Fig. 8 Connected pore level/total pore level ratio vs. crack/total pore level

IA coupled to stereological protocols on the one hand and to EIS on the other hand were implemented to quantify the coating network architecture.

Analyses permitted identification of (a) major effects of power parameters on the pore architecture and (b) related formation mechanisms.

Acknowledgments

The authors gratefully acknowledge A. Coupé from LGECO-GLISS (INSA-Strasbourg) for his valuable help in carrying out EIS experiments. LERMPS is a member of the Institut des Traitements de Surface de Franche Comté (Surface Treatment Institute of Franche Comté), France. SPCTS is the CNRS (Centre National de la Recherche Scientifique) granted research unit #6638 (France).

References

1. L. Bianchi, A. Denoirjean, F. Blein, and P. Fauchais, Microstructural Investigation of Plasma-Sprayed Ceramic Splats, *Thin Solid Films,* 1997, **299,** p 125-135
2. A.G. Evans, D.R. Mumm, J.W. Hutchinson, G.H. Meier, and F.S. Pettit, Mechanisms Controlling the Durability of Thermal Barrier Coatings, *Prog. Mater. Sci.,* 2001, **46,** p 505-553

3. J. Rösler, M. Bäker, and M. Volgmann, Stress State and Failure Mechanisms of Thermal Barrier Coatings: Role of Creep in Thermally Grown Oxide, *Acta Mater.,* 2001, **49,** p 3659-3670
4. P. Gougeon and C. Moreau, In-Flight Particle Surface Temperature Measurement: Influence of the Plasma Light Scattered by the Particles, *J. Thermal Spray Technol.,* 1993, **2**(3), p 229-233
5. C. Moreau, P. Gougeon, M. Lamontagne, V. Lacasse, G. Vaudreuil, and P. Cielo, On-Line Control of the Plasma Spraying Process by Monitoring the Temperature, Velocity and Trajectory of the In-Flight Particles, *Thermal Spray Industrial Applications,* C.C. Berndt and S. Sampath, Ed., ASM International, 1994, p 431-437
6. J.F. Coudert, M.P. Planche, and P. Fauchais, Velocity Measurement of DC Plasma Jets Based on Arc Root Fluctuations, *High Temp. Chem. Process.,* 1995, **3**(6), p 639-652
7. L. Leblanc and C. Moreau, The Long-Term Stability of Plasma Spraying, *J. Thermal Spray Technol.,* 2002, **11**(3), p 380-386
8. P. Fauchais, M. Fukomoto, A. Vardelle, and M. Vardelle, Knowledge Concerning Splat Formation: A Review, *J. Thermal Spray Technol.,* 2004, **13**(3), p 337-360
9. J. Madjeski, Solidification of Droplets on a Cold Surface, *Int. J. Heat Mass Transfer,* 1976, **19,** p 1009-1013
10. H. Fukanuma, Mathematical Modeling of Flattening Process on Rough Surfaces in Thermal Spray, *Thermal Spray: Practical Solutions for Engineering Problems,* C.C. Berndt, Ed., ASM International, 1996, p 647-656
11. M. Pasandideh-Fard, S. Chandra, and J. Mostaghimi, A Three-Dimensional Model of Droplet Impact and Solidification, *Int. J. Heat Mass Transfer,* 2002, **45,** p 2229-2242
12. G. Montavon, Z.G. Fenq, C. Coddet, Z.Q. Feng, and M. Domaszewski, Influence of the Spray Parameters on the Transient Pressure within a Molten Particle Impacting on a Flat Substrate, *Thermal Spray: A United Forum for Scientific and Technological Advances,* C.C. Berndt, Ed., ASM International, 1997, p 627-633
13. B. Glorieux, J.C. Rifflet, C. Pulvin, F. Miloot, and J.P. Coutures, Propriétés Thermodynamiques de l'Alumine Liquide (Thermodynamic Properties of Liquid Alumina), Technical Note NT1-PhC-ASSM6 CRPHT/CNRS, France, 1997, in French
14. M. Poulain, "Etude de la Conductivité Thermique de Revêtements Céramiques à Base de Zircone: Relation avec la Composition, la Microstructure et la Morphologie (Thermal Conductivity of Zirconia-Based Coatings in Relation with Composition, Phases and Porous Structure)," Ph.D. dissertation, Paris-Sud University, U.F.R. d'Orsay, France, 1999 (in French)
15. E.E. Underwood, Stereology, or the Quantitative Evaluation of Microstructures, *J. Microsc.,* 1969, **89**(2), p 161-180
16. R.T. De Hoff and F.N. Rhines, Determination of Number of Particles per Unit Volume from Measurements Made on Random Plane Sections: The General Cylinder and the Ellipsoid, *Trans. Metall. Soc. AIME,* 1961, **221,** p 975-982
17. R.T. De Hoff, The Determination of the Size Distribution of Ellipsoidal Particles from Measurements Made on Random Plane Sections, *Trans. Metall. Soc. AIME,* 1962, **224,** p 474-477
18. S.A. Saltykov, The Determination of the Size Distribution of Particles in an Opaque Material from a Measurement of the Size Distribution of their Sections, *Stereology*, H. Elias, Ed. Springer-Verlag, 1967, p 163-173
19. J. Zhang and V. Desai, Evaluation of Thickness, Porosity and Pore Shape of Plasma-Sprayed TBC by Electrochemical Impedance Spectroscopy, *Surface Coatings Technol.,* 2005, **190**(1), p 98-109
20. S. Beauvais, "Etude de l'Influence de la Porosité sur les Propriétés Électriques de Dépôts Réalisés par Projection Plasma (Influence of the Porosity on the Electrical Properties of Plasma Sprayed Coatings)," Ph.D. dissertation, Ecole Nationale Supérieure des Mines de Paris, France, 2003, in French
21. W.H. Mulder, J.H. Sluyters, T. Pajkossy, and L. Nyikos, Tafel Current at Fractal Electrodes Connection with Admittance Spectra, *J. Electroanal. Chem.,* 1990, **285**(1-2), p 103-115
22. M.C. Kaplan, A. Jégou, B. Chaufer, M. Rabiller-Baudry, and M.C. Michalsky, Adsorption of Lysozyme on Membrane Material and Cleaning with Non-Ionic Surfactant Characterized through Contact Angle Measurement, *Desalination,* 2002, **146**(1-3), p 149-154